Korea-Australia Rheology Journal, 27(4), 309-317 (November 2015) www.springer.com/13367
DOI: 10.1007/s13367-015-0030-z

Comparison of injection molding and injection/compression molding for the replication of microstructure

Seokkwan Hong[1,3], Jeongho Hwang[2], Jeongjin Kang[1,*] and Kyunghwan Yoon[3,†]
[1]*Molds & Dies R&BD Group, Korea Institute of Industrial Technology, Bucheon-si 421-742, Republic of Korea*
[2]*Micro/Nano Scale Manufacturing R&D Group, Korea Institute of Industrial Technology, Ansan-si 426-910, Republic of Korea*
[3]*Department of Mechanical Engineering, Dankook University, Yongin-si, Republic of Korea*
(Received August 13, 2015; final revision received October 22, 2015; accepted October 31, 2015)

Because of increasing interest in the functional surfaces including micro- or nano-patterns, the mass production of such surfaces has been actively researched. Both conventional injection molding (CIM) and injection/compression molding (ICM) of micro-patterns were investigated in the present study. The molding subject is a multi-scale structure that consists of a macro-scale thin plate and micro-scale patterns formed regularly on its surface. The transcription ratios of micro pattern made by CIM and ICM for different flow length were experimentally measured, and the origin of the obtained results was identified through numerical analysis. It was found that the cavity pressure and polymer temperature are the most important factors for micro-pattern filling; in particular, the polymer temperature is the key factor determining the transcription ratio. It was also found that the difference in CIM and ICM micro-pattern transcription ratios originates from the differences in the cavity pressure history if other molding conditions are the same.

Keywords: micro-pattern, injection/compression molding, injection molding, dual-domain method, phase field method

1. Introduction

Studies of the micro- or nano-patterned functional surfaces have been actively conducted in various fields(Liu and Jiang, 2011). In particular, biomimetics is one representative area of research that has seen an increased number of studies of such surfaces. The superhydrophobic function of the lotus leaf surface, structural color of the *Morpho-peleides* butterfly wing surface, anti-reflective function of the moth-eye surface, and dry adhesive function of the gecko sole are examples of biomimetics attracting intense interest in this field. The randomly or regularly distributed nano- or micro-scale projections form independently or through a complex process on the surfaces of these organisms. The surface function depends on the shape, structure, and distribution of these micro-projections (or patterns) (Liu and Jiang, 2011). Because these surface functionalities are highly useful, there are ongoing attempts to develop imitations of these surfaces for use in the industry and technology. However, the mass production of such surfaces is difficult because efficient methods for manufacturing the micro-scale or nano-scale patterns are unavailable at present.

In this study, we focus on the molding of thermoplastic polymers. Here, the current common micro-pattern molding methods include micro injection molding, hot embossing, and micro thermoforming (Heckele and Schomburg, 2003). Among these molding methods, injection molding is suitable for mass production because of its relatively short cycle time and high repeatability and reproducibility. These advantages have motivated recent active research to produce functional products, including micro-patterns with injection molding (Yang *et al*., 2013).

However, injection molding also exhibits several characteristics that are unfavorable for the replication of the micro-patterns (Hong *et al*., 2015).

i) The solidification phenomenon occurs when the polymer melt contacts the relatively cold mold surface; this makes it difficult to charge a polymer melt into a micro-scale cavity. ii) Pressure deviation along the flow length within the cavity causes non-uniform micro-pattern transcription over the entire molding area. To overcome these limitations, molding methods that add special functions to conventional injection molding (CIM) such as injection/compression molding (ICM) have been already proposed and developed for a long time. ICM is advantageous for achieving thickness uniformity and dimensional accuracy.

A concept of combining injection molding and compression molding was first proposed when Klepek (*Klepek*, 1987) and Matsuda *et al*. (Matsuda *et al*., 1985) molded a thick optical lens and Yang *et al*. (Yang and Ke, 1995) proved this effect by systematic experiments. The biggest advantage of ICM is that uniform pressure is applied to polymer filled in the cavity in the compression stage. This reduces the injection pressure and clamp force (Isayev,

*Corresponding author; E-mail: doublej@kitech.re.kr
†Co-Corresponding author; E-mail: khyoon@dankook.ac.kr

2000; Osswald *et al.*, 2008) and favorably affects the molded parts' properties, for example, leading to residual stress reduction, polymer orientation and birefringence reduction, high dimensional accuracy and warpage reduction, and uniform shrinkage (Huang *et al.*, 2008; Yang and Chen, 1998; Chen *et al.*, 2000, Min and Yoon, 2011). On the other hand, only a few papers have studied the effects on micro-pattern molding, *e.g.*, Shen (2007) and Ito and Suzuki (2009) examined the dependence of the micro-pattern molding properties on CIM and ICM conditions.

In the present paper the relationships between the micro-pattern molding properties and ICM conditions using numerical analysis were investigated. The use of numerical analysis allowed us to more thoroughly explain the effects of the ICM process on the filling of micro-patterns. To further clarify these effects, the results of numerical analysis for ICM were compared with experimental data.

2. Experimental

As shown in Fig. 1, the molding subject has the sheet shape with the width, length, and nominal thickness of 160 mm, 90 mm, and 1.12 mm, respectively. The micro-pattern is cylindrically shaped with a diameter and height

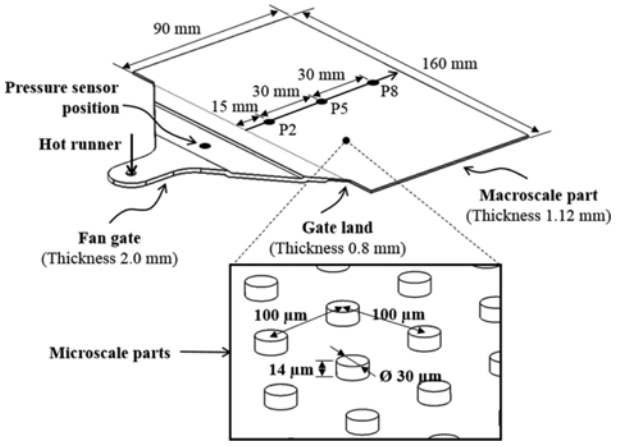

Fig. 1. Schematic diagram of the multi-scale components for injection molding: P2, P5 and P8 denote the measurement locations that are 15, 45 and 75 mm, respectively away from the gate (Hong *et al.*, 2014).

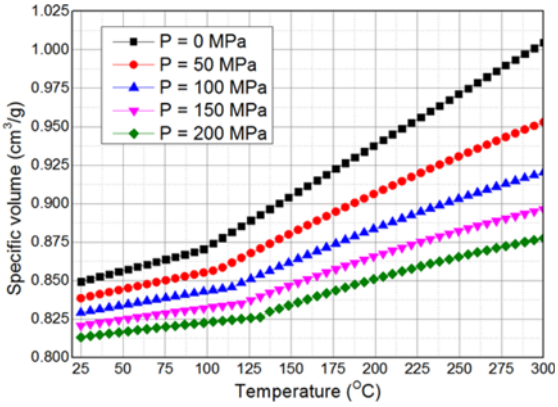

Fig. 2. (Color online) PVT diagrams of PMMA (TF8) (Moldflow).

of 30 μm and 14 μm, respectively and a 100 μm gap between the patterns. The pattern was uniformly distributed throughout the area. PMMA TF8 (melt flow rate (MFR) of 10.0 g/10 min at 230°C, 37.3 N) of Mitsubishi Rayon was used for the polymer resin. As shown in Fig. 2, the glass transition temperature of this resin is 105°C. An injection molding machine used in this study (LS Mtron Co., Ltd, Korea) consists of an in-line screw-type injection unit and a toggle-type clamping unit. The mold structure and process conditions are shown in Fig. 3 and Table 1. In the ICM process, the process conditions of the injection stage are the same as those of CIM, while the

Table 1. Experimental conditions for different molding processes.

Factor	Set point	Processes	
		CIM	ICM
Mold temperature (°C)	80	√	√
Injection speed (mm/s)	140	√	√
Injection time (s)	0.43	√	√
Cooling time (s)	25	√	√
Hot runner temperature (°C)	270	√	√
Packing pressure (MPa)	50	√	
Packing time (s)	3	√	
Mold open distance (mm)	0.1		√
Compressing force (MN)	1.078 (110 tf)		√

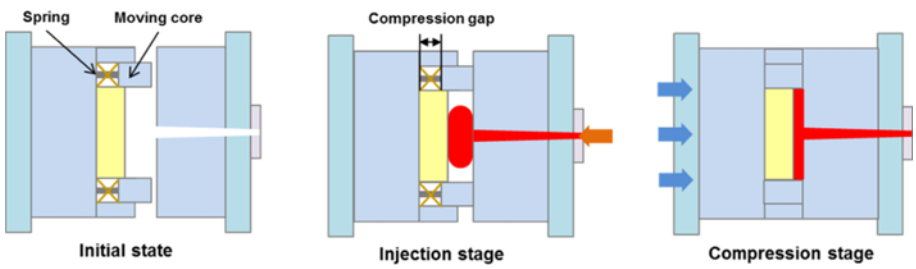

Fig. 3. (Color online) Operating principle of moving core during injection compression process.

those of CIM. A more detailed description of the experimental method can be found in previous studies (Hong *et al*., 2014).

3. Numerical Model

In the polymer injection molding simulation, two techniques are generally used for simulating the part where the cavity of macro-scale and micro-scale co-exists. One approach is to treat the entire multi-scale cavity as one domain (Shen *et al*., 2008). Alternatively, the cavity can be separated to domains that are coupled with each other (Kim and Turng, 2006). While both these approaches have advantages and disadvantages, it is clear that the latter method (dual-domain method, DDM) is more suitable as the pattern becomes smaller and surface area of moldings becomes larger. Therefore, in the present study, simulation was performed for the behavior of the micro-pattern filled during ICM using a DDM-based technique developed in a previous study (Hong *et al*., 2015). However, the boundary conditions applied to the packing stage are different from those of the previous study because only CIM was modeled in the previous study.

As a first step the filling simulation of a macro-scale model was performed, the simulation for the assumed part without the micro-scale patterns, using the commercial Moldflow software. The purpose of this simulation was to obtain cavity pressure data over time at an arbitrary position to be used as a boundary condition in the micro-scale filling model.

Next, the filling simulation of a micro-scale model, which is the filling simulation for one pattern, was performed. As shown in Fig. 4, here, the size of the micro-scale domain corresponds to the area occupied by one pattern ($x = 0.1$ mm, $y = 0.1$ mm) in the flow direction of the polymer melt and to the area from the cooling channel center of the fixed-side mold to the cooling channel center of the moving-side mold in the vertical direction. In this area, polymer, stamper, core, and cooling channel are included and heat exchange between each layer is considered. The COMSOL Multiphysics software was used for this micro-scale filling simulation. The micro-scale filling behavior of polymer melt is assumed to follow laminar flow of incompressible and viscous fluid. This motion can be described by the incompressible Navier-Stokes equation and the continuity equation.

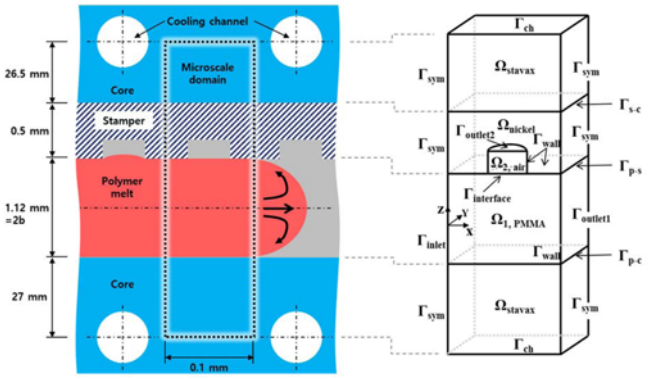

Fig. 4. (Color online) Domain of the micro-scale filling model and the boundary conditions (Hong *et al*., 2015).

$$\rho\frac{\partial \mathbf{u}}{\partial t}+\rho(u\cdot\nabla)u=\nabla\cdot\left[-p\mathbf{I}+\eta\left(\nabla\mathbf{u}+(\nabla\mathbf{u})^{T}\right)\right]+\mathbf{F}_{st}+\rho\mathbf{g}, \quad (1)$$

$$\nabla\cdot\mathbf{u}=0 \quad (2)$$

where p is the pressure, $\mathbf{I}$ is the identity matrix, $\mathbf{g}$ is the gravity vector, and $\mathbf{F}_{st}$ is the surface tension acting between the air and polymer. ρ, η and $\mathbf{u}$ denote the density, dynamic viscosity and fluid velocity, respectively.

The energy equation for the fluid including heat transfer by convection and conduction is given as follows:

$$\rho C_P\frac{\partial T}{\partial t}+\rho C_P\mathbf{u}\cdot\nabla T=\nabla\cdot(k\nabla T)+Q \quad (3)$$

where C_P indicates specific heat capacity, T is the temperature, k is the heat conductivity, and Q is a heat source such as shear heating. To track the moving interface between the polymer melt and air, the phase field method (PFM) (Yue *et al*., 2004) based on the Cahn-Hilliard equation (Cahn and Hilliard, 1958) was applied. Here, the interface is separated into areas from −1 to 1 by the dimensionless phase field variable ϕ, as shown in the equation below.

$$\frac{\partial\phi}{\partial t}+\mathbf{u}\cdot\nabla\phi=\nabla\cdot\frac{\gamma\lambda}{\varepsilon^{2}}\nabla\psi\ , \quad (4)$$

$$\psi=-\nabla\cdot\varepsilon^{2}\nabla\phi+(\phi^{2}-1)\phi \quad (5)$$

where t indicates time, γ is the mobility, λ is the mixing energy density, ψ is the phase field help variable, and ε is the interface thickness parameter. The volume fraction of each fluid, V_f, is given as follows:

$$V_{f1}=\frac{1-\phi}{2},V_{f2}=\frac{1+\phi}{2}. \quad (6)$$

In this simulation, the polymer melt was defined as Fluid 1 and air as Fluid 2. The material properties of each fluid, ρ, η, C_P, and k, smoothly express the material properties of the mixture at the interface as follows:

$$\rho=\rho_{pm}+(\rho_{air}-\rho_{pm})V_{f2}, \quad (7)$$

$$\eta=\eta_{pm}+(\eta_{air}-\eta_{pm})V_{f2}, \quad (8)$$

$$k=k_{pm}+(k_{air}-k_{pm})V_{f2}, \quad (9)$$

$$C_P=C_{P,pm}+(C_{P,air}-C_{P,pm})V_{f2}. \quad (10)$$

Here, the physical property of the polymer melt is denoted by the subscript pm and that of the air by the subscript air. The viscosity of the air was assumed to be constant and independent of the temperature and pressure to increase the stability of the solution because air only has a slight effect on the motion of the polymer melt. On the other hand, the Cross-WLF viscosity model that shows dependence on the temperature and shear rate was applied to polymer melt. The polymer melt viscosity was given as follows:

$$\eta = \frac{\eta_0}{\left[1+\left(\frac{\eta_0\dot{\gamma}}{\tau^*}\right)^{1-n}\right]}, \tag{11}$$

$$\eta_0 = D_1 \exp\left(-\frac{A_1\left(T-T^*\right)}{A_2+\left(T-T^*\right)}\right) \tag{12}$$

where η_0 denotes the zero-shear viscosity, $\dot{\gamma}$ is the shear rate, τ^* is the critical stress level at the transition to shear thinning, n is the power law index in the high shear rate regime, T^* is the glass transition temperature, and D_1, A_1, A_2 are material constants. The viscosity (η) of the polymer melt and material properties of each layer are shown in Fig. 5 and Table 2, respectively. Facets of structural behavior such as elastic deformation of the solidified layer were not considered in the present study. Therefore, the solidification of the polymer melt refers to the flow-stop condition, which depends on the viscosity of the polymer, as shown in Fig. 5.

The initial state of the micro-scale model is assumed to correspond to the moment when the polymer melt just passes the micro cavity. Therefore, the initial temperature of polymer melt was set to 270°C, and the injection temperature (T_{inj}) and the initial temperatures of air, stamper, and core were set to the mold temperature (T_{mold}), 80°C.

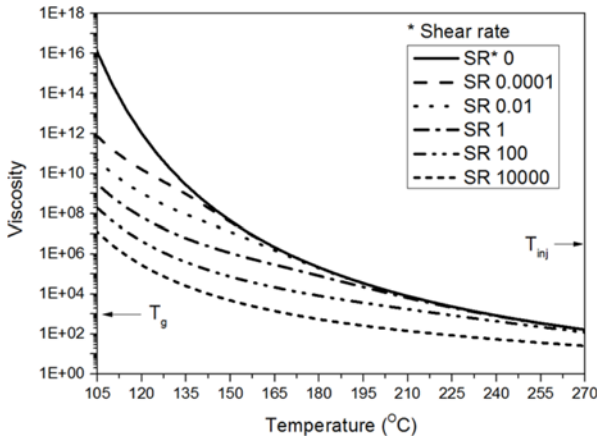

Fig. 5. Viscosity as a function of temperature and shear rate for PMMA (TF8) (Moldflow).

Table 2. Material properties for micro-scale filling analysis.

Factor	PMMA (polymer melt)	Air	Nickel (stamper)	STAVAX (core)	Unit
P	1000	1	8800	7740	kg/m^3
K	0.19	0.023	60.7	20	W/m K
C_p	2200	1004	460	460	J/kg K
τ^*	95093.9	-	-	-	Pa
n	0.4053	-	-	-	-
T^*	377.15	-	-	-	K
D_1	2.599×10^{16}	-	-	-	Pa·s
A_1	42.849	-	-	-	-
A_2	51.6	-	-	-	K

$$V_{f2} = \begin{Bmatrix} 1 \text{ for } z > 0.56 \text{ mm} \\ 0 \text{ for } z < 0.56 \text{ mm} \end{Bmatrix}$$

$$\forall\left(x,y,z,t=0\right) \in \Omega_{PMMA} \cup \Omega_{air}, \tag{13}$$

$$T = T_{inj} \qquad \forall\left(x,y,z,t=0\right) \in \Omega_{PMMA}, \tag{14}$$

$$T = T_{mold} \qquad \forall\left(x,y,z,t=0\right) \in \Omega_{air} \cup \Omega_{nickel} \cup \Omega_{stavax}, \tag{15}$$

$$\mathbf{u} = 0 \qquad \forall\left(x,\mathrm{y},z,t=0\right) \in \Omega_{PMMA} \cup \Omega_{air}. \tag{16}$$

In the injection stage, mass flow at the rate $\dot{m}$ is supplied to the inlet (Γ_{inlet}). The actual cavity pressure changes in real time at that position are reflected using the pressure $p(t)$ obtained from macro-scale filling simulation at the outlet ($\Gamma_{outlet1}$). In the compression stage, the velocity conditions applied to inlet (Γ_{inlet}) are switched to the pressure conditions (VPSO) and the outlet ($\Gamma_{outlet1}$) conditions are switched to the wall conditions. In addition, to simulate the process of complete closure of the moving mold opened in advance for compression, both Γ_{wall} ($z = -0.56$) and Γ_{ch} ($z = -27.56$) correspond to the movable mold movement at the same time and the same speed in the y-direction. At this time, the moving distance is 0.1 mm and the speed is 0.33 mm/s. Furthermore, outlet ($\Gamma_{outlet2}$) for venting air in the micro cavity continues to maintain the opened state during the injection and packing stage for improving the convergence of the solution. Therefore, compression of the air as the polymer is filled was not considered. This omission is supported by the study of Lin and Young (2009) who showed that the effect of trapped air can be ignored in the micro injection molding. However, this assumption is limited to the size of the pattern used in this study. The mass flow is given as follows:

$$\dot{m} = \rho_{pm} u_m A_{mi} \quad \forall\left(x=0,y,z,t=\text{filling stage}\right) \in \Gamma_{inlet}, \tag{17}$$

$$p = p\left(t\right) \quad \begin{Bmatrix} \forall\left(x=0.1\text{ mm},y,z,t=\text{filling stage}\right) \in \Gamma_{outlet1} \\ \forall\left(x=0,y,z,t=\text{compression stage}\right) \in \Gamma_{inlet} \end{Bmatrix}, \tag{18}$$

$$\mathbf{u} = 0 \quad \forall\left(x=0.1\text{ mm},y,z,t=\text{compression stage}\right) \in \Gamma_{outlet1}, \tag{19}$$

where ρ_{pm} is obtained from the density (1000 kg/m^3) at the initial temperature (T_{inj} = 270°C) of the polymer and u_m is obtained from the macro-scale filling rate as the average velocity (0.35 m/s) of the thickness direction at that position. A_{mi} is the area (5.6×10^{-8} m^2) of inlet (Γ_{inlet}). The no-slip condition is used for all walls, and the symmetry condition is given for the y = 0 and 0.05 mm position in the fluid area according to

$$\mathbf{u} = 0 \qquad \forall(x,y,z,t) \in \Gamma_{wall}, \tag{20}$$

$$\left.\begin{array}{l}\mathbf{u}\cdot\mathbf{n} = 0 \\ \boldsymbol{\tau} = 0\end{array}\right\} \quad \left\{\begin{array}{c}\forall(x, y=0, z, t) \\ \forall(x, y=0.05\ \text{mm}, z, t)\end{array}\right\} \in \Gamma_{sym}. \tag{21}$$

In the micro-scale domain, the temperature of inlet (Γ_{inlet}) is set for all T_{inj} in the z direction for t = 0. However, shortly later, the temperature of the inlet (Γ_{inlet}) is synchronized with the temperature of the outlet (Γ_{outlet}).This is to take into account the temperature of the polymer melt continuously incoming from the upstream of the current position.

$$T(x=0) = T(x=0.1\,\text{mm}) \quad \forall(x=0,y,z,t) \in \Gamma_{inlet}. \tag{22}$$

Micro-patterns are repeatedly arranged while maintaining regular intervals. Therefore, symmetric heat transfer boundary conditions are applied to Γ_{sym} in the stamper and core.

$$-k\left|\frac{\partial T}{\partial z}\right| = 0 \qquad \left\{\begin{array}{c}\forall(x=0,y,z,t) \\ \forall(x,y=0,z,t) \\ \forall(x=0.1\,\text{mm},y,z,t) \\ \forall(x,y=0.1\,\text{mm},z,t)\end{array}\right\} \in \Gamma_{sym}. \tag{23}$$

Forced convection heat transfer conditions by the cooling channel are used for the top (z = 27.56 mm) and bottom (z = −27.56 mm) surfaces of the simulation model.

$$-k\left|\frac{\partial T}{\partial z}\right| = h_{c-c}\cdot(T_{cw} - T_{core}) \qquad \left\{\begin{array}{c}\forall(x,y,z=27.56\,\text{mm},t) \\ \forall(x,y,z=-27.56\,\text{mm},t)\end{array}\right\} \in \Gamma_{ch}, \tag{24}$$

$$-k\left|\frac{\partial T}{\partial z}\right| = \frac{1}{R_{p-s}}\left(T_{pm} - T_s\right) \quad \forall(x,y,z=0.56\,\text{mm},t) \in \Gamma_{p-s}. \tag{25}$$

Here, T_{cw}, T_{core}, T_{pm}, and T_s denote the temperatures of cooling water, core, polymer melt, and stamper, respectively. The heat transfer coefficient h_{c-c} and thermal contact resistance coefficient (TCRC) R_{p-s} between the polymer and stamper are specified following the approach described in our previous study (Hong *et al.*, 2015), as will be discussed later.

In this micro-scale model, the tetrahedral element was adopted for domain discretization. The total number of elements and degrees of freedom are 72,144 and 165,501, respectively. The linear elements of both the velocity components and pressure field were selected to improve numerical robustness. An effective solver called a parallel sparse direct solver was used to improve the calculation speed and memory management.

4. Results and Discussion

4.1. Transcription ratio of micro-pattern

Fig. 6 shows experimental results for the transcription ratios of micro-pattern made by CIM and ICM at various distances from the gate. In CIM, the transcription ratio was approximately 93.6% near the gate and approximately 2.6% at the farthest distance from the gate. Compared with CIM, transcription was generally increased in the case of ICM. In particular, unlike CIM that showed a rapidly decreasing transcription at increasing distances away from the gate, the transcription ratio of approximately 40% was maintained at the farthest distance. The purpose of this study is to describe the following two major phenomena. First, the micro-pattern transcription of CIM falls sharply far away from the gate. Second, in the case of ICM, transcription was improved, although the temperature of the mold is the same as that of CIM.

4.2. Velocity distribution

The most important feature of ICM is the modeling of the injection stage while the mold is not completely closed. Thus, the velocity of the polymer melt is generally reduced because of the effect of larger cavity thickness. In this simulation, mold-open distance was set to 0.1 mm (9% of the thickness). The results of the simulation are presented in Fig. 7 and show the velocity change of the polymer melt over time at P5. Examination of Fig. 7 also shows that the solidification layer of polymer melt (veloc-

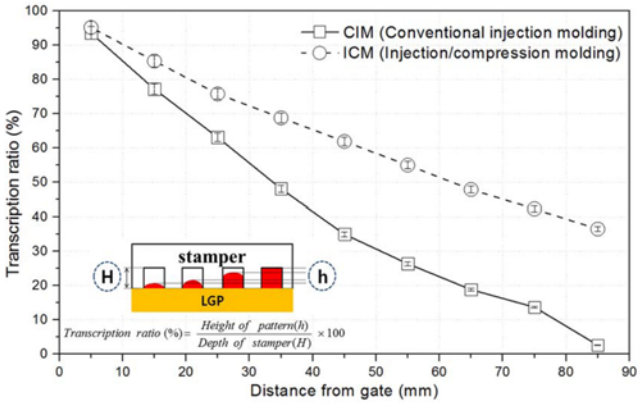

Fig. 6. (Color online) Experimental results for transcription ratio of micro-patterns at various distances from the gate for different molding processes.

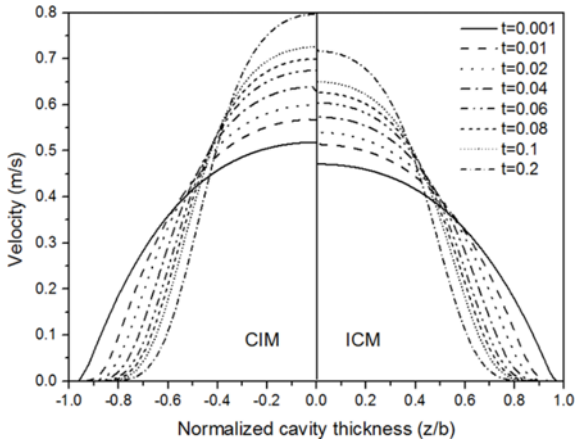

Fig. 7. Simulation results of velocity profiles for CIM and ICM at P5.

ity ≅ 0) grows increasingly thick near the wall of mold over time. This causes the flow channel to be gradually narrowed and the flow velocity to increase. The flow velocity affects the thickness of the solidification layer and the gradient of cavity pressure, and this affects the filling behavior of micro-pattern. The maximum flow velocity in the cavity center was predicted to be 0.8 m/s and 0.7 m/s in CIM and ICM, respectively. As described later, this difference was found to hardly affect the filling of the micro-pattern.

4.3. Temperature distribution

It is obvious that the cavity pressure and temperature of the polymer have the greatest impact on the filling of the micro-pattern in CIM (Yu *et al*., 2002; Su *et al*., 2004; Young, 2005; Tofteberg *et al*., 2008; Kuhn *et al*., 2010). The temperature distributions of the polymer for different times in CIM and ICM are shown in Fig. 8. It can be seen that starting at the initial temperature of 270°C, the polymer melt is rapidly cooled from the time of contact with the relatively cold mold surface near the mold surface. On the other hand, the initial polymer temperature is maintained in the cavity center. The influence of shear heating also can be seen, and in the case of ICM, the heat generation rate can be seen to be slightly smaller than that for CIM because of the speed reduction mentioned above.

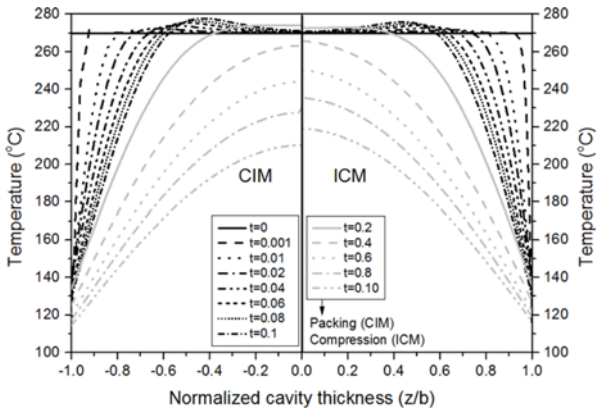

Fig. 8. Simulation results of temperature profiles between CIM and ICM at P5: Black line represents "filling stage" and gray line represents "packing or compression stage".

4.4. Cavity pressure

Cavity pressure is the pressure formed in the cavity during injection molding. This pressure serves as a driving force for the filling of the polymer melt into the micro-scale cavity. The cavity pressure and the average temperature (T_a) predicted by the simulations are shown in Fig. 9. First, the pressure values obtained in both CIM and ICM increased at the almost the same rate to reach the velocity/pressure switch-over (VPSO) value at P2; the two methods then showed significant differences in the obtained pressure during the packing and compression stage. Prior to VPSO, the conditions in CIM and ICM are the same; therefore, the obtained cavity pressure values are the same. In fact, strictly speaking, the pressure of ICM is slightly smaller because of the influence of the opened mold.

Examination of the changes in T_a (Fig. 9a) shows that T_a is essentially instantaneously reduced from the initial temperature of 270°C to 145°C. The cooling rate then decreases

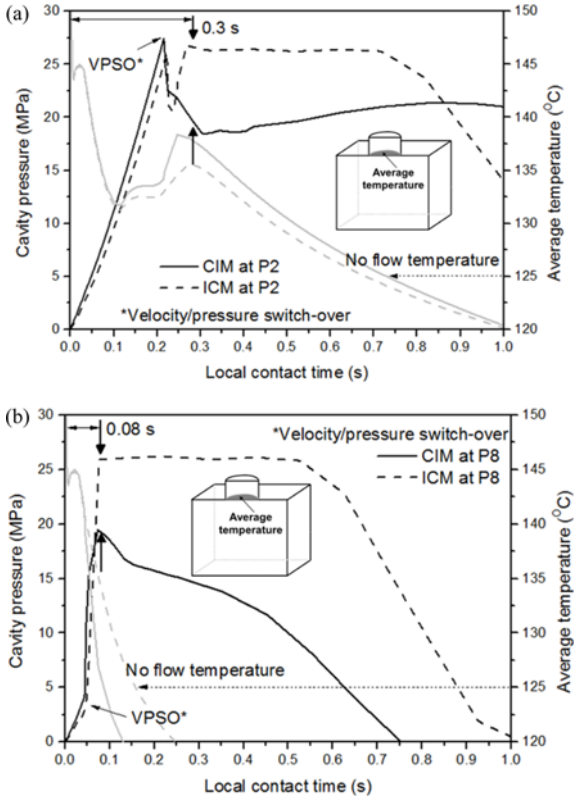

Fig. 9. Simulation results of cavity pressure profiles at (a) P2 and (b) P8: Black line represents "cavity pressure" and gray line represents "average temperature".

because of the continuous supply of high-temperature polymer melt, leading to reheating after 0.1 s. This is the main cause for the first of the above phenomena. Changes in T_a at P8 show a significant difference from those at P2. There is no reheating, and the time (0.15 s) to no flow temperature (the temperature for which the micro-pattern filling rate becomes 0) is also much shorter. In fact, this is a more favorable condition for the micro-pattern filling because the gradient of the cavity pressure increases more steeply at this point (P8) than at P2. Nevertheless, the micro-pattern filling amount is significantly lower because of the much faster polymer solidification at P8 than at P2. It is obvious that an increase in the cavity pressure in this condition will increase the micro-pattern transcription ratio. In a situation where the temperature changes in CIM and ICM are not significantly different, the transcription improvement in micro-pattern results from higher cavity pressure of ICM. This is the explanation for the second phenomenon.

As shown in Fig. 6, the transcription ratio for the case of ICM was 40% at the end of the gate, and it can be inferred from these simulation results that the following methods can be used to increase this value:

(i) Raise the temperature of the mold. While this is the most effective way to lower the viscosity of polymer, this approach has a drawback of a prolong cycle time. (ii) Increase the injection speed. This allows VPSO to start at the higher temperature, thereby guaranteeing a longer packing time until the no flow temperature is reached. (iii) Increase the cavity pressure. Cavity pressure during the compression stage in ICM can be increased by either filling more polymer melt or increasing the speed of closing the mold. The former is closely related to the thickness and weight of the product. The latter is effective only when the movable mold is closed faster than the rate at which the polymer filled in the cavity is cooled and contracted.

Finally, the experimental results and simulation results for filling behavior of micro-pattern over time were compared as shown in Fig. 10. The lines are from numerical simulation and the symbols are obtained from experiments as shown in Fig. 6. Time history for the filling height of the pattern was measured numerically by the indirect method. Thermal contact resistance (TCR) was obtained by matching these measured results with simulation results, and the discussion for TCR was published in present authors' other paper (Hong *et al*., 2015). Filling behavior at the farthest distance from the gate (P8) is noteworthy in these results. VPSO time decreases as the distance from the gate is increased. This implies a drastic buildup of the cavity pressure directly after VPSO begins before the polymer melt is frozen. Under this condition, in ICM, the cavity pressure is higher and is maintained for a longer time than in the case of CIM, as shown in Fig. 9. These differences led to a remarkable filling height in micro-patterns made using ICM at P8, as shown in Fig. 10b.

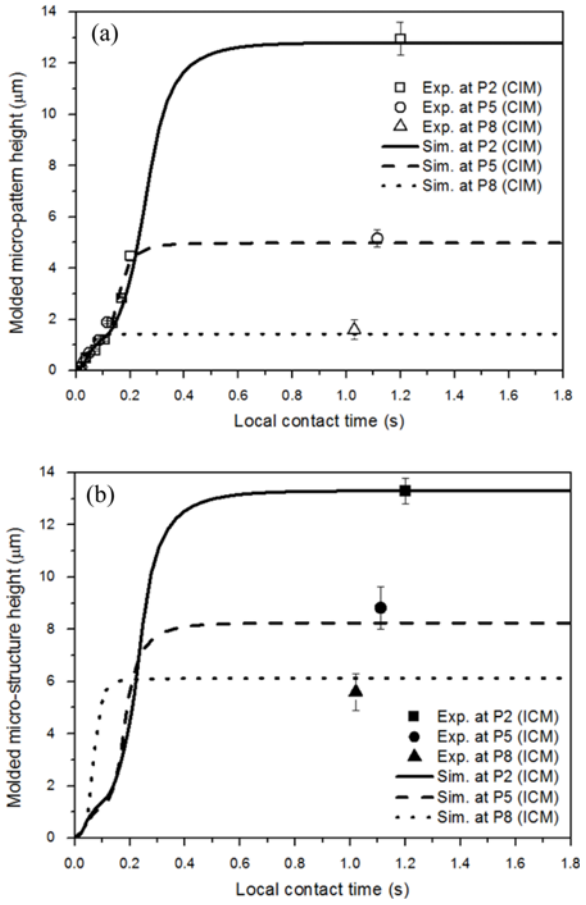

Fig. 10. Comparison of molded micro-feature height between numerical and experimental results at various distances from gate: (a) CIM and (b) ICM.

5. Conclusions

In order to explain the effect of CIM and ICM processes on the micro-pattern filling behavior, experimental measurements and numerical simulations were performed. For both CIM and ICM, it is obvious that the cavity pressure and temperature of the polymer are the most important factors in micro-pattern filling. A pattern is successfully filled only when both the cavity pressure and polymer temperature are set at appropriate values. Even for extremely high cavity pressures, the pattern cannot be filled normally if the temperature of the polymer does not satisfy the conditions for flowing. On the other hand, even for very high polymer temperatures, the non-filling of the pattern will be obtained if the cavity pressure is not maintained continuously. In light of these facts, the following results were obtained in the present study: (i) Solidification of the polymer proceeded faster farther away from the gate. This

is the main cause for the lower micro-pattern transcription ratios at larger distances from the gate. (ii) The temperature history of the polymer is almost the same in CIM and ICM. (iii) The polymer temperature reached the no flow temperature within the packing stage in CIM and within the compression stage in ICM. That is, the micro-pattern filling flow stopped even for non-zero cavity pressure. (iv) The improvement in micro-pattern filling in ICM is only due to the difference in cavity pressures. Finally, we hope that the results of this study will help to advance the commercialization of the functional surface.

Acknowledgments

This work was financially supported by the Ministry of Planning and Budget and Korea Institute of Industrial Technology (Project No. JG150009) and the Ministry of Knowledge and Economy (Project No. 10033710).

List of Symbols

A_1 : Material constant 1
A_2 : Material constant 2 (K)
A_{mi} : Cross-sectional area of micro-scale inlet (m^2)
C_P : Specific heat capacity (J/kg K)
$\mathbf{D}$: Strain rate tensor
D_1 : Material constant 1 (Pa·s)
$\mathbf{F}_{st}$: Surface tension force acting at the air/polymer melt interface (N)
$\mathbf{g}$: Gravity vector (m/s^2)
h : Contact heat transfer coefficient (W/m^2 K)
$h_{c\text{-}c}$: Contact heat transfer coefficient between cooling water and core (W/m^2 K)
$\mathbf{I}$: Identify tensor
k_{air} : Thermal conductivity of air (W/m K)
k_{core} : Thermal conductivity of core (W/m K)
k_{cw} : Thermal conductivity of cooling water (W/m K)
k_{pm} : Thermal conductivity of polymer melt (W/m K)
k_s : Thermal conductivity of stamper (W/m K)
$\dot{m}$: Rate of mass flow (kg/s)
n : Power law index in the high shear rate regime
p : Pressure (Pa)
Q : Heat source (J)
$R_{p\text{-}s}$: Thermal contact resistance coefficient between polymer and stamper (m^2 K/W)
t : Time (s)
T : Temperature (°C)
T^* : Glass transition temperature (°C)
T_0 : Initial air temperature (°C)
T_{core} : Temperature of core (°C)
T_{cw} : Temperature of cooling water (°C)
T_{inj} : Temperature of injected polymer melt (°C)
T_{mold} : Temperature of mold (°C)
T_{pm} : Temperature of polymer melt (°C)
T_s : Temperature of stamper (°C)
u : Fluid velocity (m/s)
u_m : Mean velocity (m/s)
V_{f1} : Volume fraction of fluid 1
V_{f2} : Volume fraction of fluid 2

Greek symbols

Γ_{inlet} : Inlet in the micro-scale domain
Γ_{outlet} : Outlet in the micro-scale domain
$\dot{\gamma}$: Shear rate
$\dot{\boldsymbol{\gamma}}$: Shear rate tensor
ε : Interface thickness parameter (m)
ζ : Surface tension of polymer melt (N/m)
η_0 : Zero shear viscosity (Pa·s)
η_{air} : Dynamic viscosity of air (Pa·s)
η_{pm} : Dynamic viscosity of polymer melt (Pa·s)
λ : Mixing energy density (N)
ρ_{air} : Density of air (kg/m^3)
ρ_{cw} : Density of cooling water (kg/m^3)
ρ_{pm} : Density of polymer melt (kg/m^3)
$\boldsymbol{\sigma}^*$: Total stress tensor
τ^* : Critical stress level at the transition to shear thinning (Pa)
$\boldsymbol{\tau}$: Shear stress
ψ : Phase field help variable
Φ : Phase field variable

Subscripts

cc : Cooling channel
c-c : Between cooling water and core
cw : Cooling water
*f*1 : Fluid 1 (polymer melt)
*f*2 : Fluid 2 (air)
inj : Injection
m : Mean
mi : Micro-scale inlet
pm : Polymer melt
p-s : Between polymer and stamper
s : Stamper
st : Surface tension

References

Cahn, J.W. and J.E. Hilliard, 1958, Free energy of a nonuniform system. I. Interfacial free energy, *J. Chem. Phys.* **28**, 258-267.

Chen, S.C., Y.C. Chenand, and H.S. Peng, 2000, Simulation of injection-compression-molding process. II. Influence of process characteristics on part shrinkage, *J. Appl. Polym. Sci.* **75**, 1640-1654.

Heckele, M. and W.K. Schomburg, 2003, Review on micro molding of thermoplastic polymers. *J. Micromech. Microeng.* **14**, R1-R14.

Hong, S., I. Min, K. Yoon, and J. Kang, 2014, Effects of adding injection-compression to rapid heat cycle molding on the structure of a light guide plate, *J. Micromech. Microeng.* **24**, 015009.

Hong, S., J. Kang, and K. Yoon, 2015, Correlation between thermal contact resistance and filling behavior of a polymer melt into multiscale cavities in injection molding, *Int. J. Heat Mass Transf.* **87**, 222-236.

Huang, H.-X., K. Li, and S. Li, 2008, Injection-compression molded part shrinkage uniformity comparison between semicrystalline and amorphous plastics, *Polym. Plast. Technol. Eng.* **48**, 64-68.

Isayev, A.I., 2000, Molding processes, In: L.S. Richard and L.H. Ernest, eds., *Handbook of Industrial Automation*, CRC Press, Boca Raton, 573-606.

Ito, H. and H. Suzuki, 2009, Micro-features formation in injection compression molding, *J. Solid Mech. Mater. Eng.* **3**, 320-327.

Kim, S. and L. Turng, 2006, Three-dimensional numerical simulation of injection molding filling of optical lens and multiscale geometry using finite element method, *Polym. Eng. Sci.* **46**, 1263-1274.

Klepek, G., 1987, Herstellung optischer Linsen im Spritzprägeverfahren, *Kunststoffe* **77**, 1147-1151.

Kuhn, S., A. Burr, M. Kubler, M. Deckertand, and C. Bleesen, 2010, Study on the replication quality of micro-structures in the injection molding process with dynamical tool tempering systems, *Microsyst. Technol.* **16**, 1787-1801.

Lin, H.-Y. and W.-B. Young, 2009, Analysis of the filling capability to the microstructures in micro-injection molding, *Appl. Math. Model.* **33**, 3746-3755.

Liu, K. and L. Jiang, 2011, Bio-inspired design of multiscale structures for function integration, *Nano Today* **6**, 155-175.

Matsuda, S., A. Itoh, and T. Tamura, 1985, (No Title), *Natl. Tech. Rep.*, **14**, 641.

Min, I.K. and K. Yoon, 2011, An experimental study on the effects of injection-molding types for the birefringence distribution in polycarbonate discs, *Korea-Aust. Rheol. J.* **23**, 155-162.

Osswald, T.A., L.S. Turng, and P.J. Gramann, 2008, *Injection Molding Handbook*, Hanser Verlag, Munich.

Shen, Y.K., 2007, Comparison of height replication properties of micro-injection moulding and micro-injection-compression moulding for production of microstructures on lightguiding plates, *Plast. Rubber Compos.* **36**, 77-84.

Shen, Y.K., C.Y. Chang, Y.S. Shen, S.C. Hsuand, and M.W. Wu, 2008, Analysis for microstructure of microlens arrays on micro-injection molding by numerical simulation, *Int. Commun. Heat Mass Transf.* **35**, 723-727.

Su, Y.-C., J. Shah, and L. Lin, 2004, Implementation and analysis of polymeric microstructure replication by micro injection molding, *J. Micromech. Microeng.* **14**, 415.

Tofteberg, T., H. Amédro, and E. Andreassen, 2008, Injection molding of a diffractive optical element, *Polym. Eng. Sci.* **48**, 2134-2142.

Yang, C., X.-H. Yin, and G.-M. Cheng, 2013, Microinjection molding of microsystem components: new aspects in improving performance, *J. Micromech. Microeng.* **23**, 093001.

Yang, S.Y. and Y.C. Chen, 1998, Experimental study of injection-charged compression molding of thermoplastics, *Adv. Polym. Technol.* **17**, 353-360.

Yang, S.Y. and M.Z. Ke, 1995, Experimental study on the effects of adding compression to injection molding process, *Adv. Polym. Technol.* **14**, 15-24.

Young, W.B., 2005, Simulation of the filling process in molding components with micro channels, *Microsyst. Technol.* **11**, 410-415.

Yu, L., C.G. Koh, L.J. Lee, K.W. Koelling, and M.J. Madou, 2002, Experimental investigation and numerical simulation of injection molding with micro-features, *Polym. Eng. Sci.* **42**, 871-888.

Yue, P., J.J. Feng, C. Liu and J. Shen, 2004, A diffuse-interface method for simulating two-phase flows of complex fluids, *J. Fluid Mech.* **515**, 293-317.